Inorganic Chemistry

pubs.acs.org/IC

Article

Multi-functional Single-Source Molecular Precursors for Carbon-Coated Mixed-Metal Phosphates

Haixiang Han, Yuxuan Zhang, Zheng Zhou, Jesse C. Carozza, Zheng Wei, Alexander S. Filatov, Andrey Shevtsov, Artem M. Abakumov, and Evgeny V. Dikarev*

Cite This: *Inorg. Chem.* 2023, 62, 12931−12939

Read Online

ACCESS | Metrics & More | Article Recommendations | Supporting Information

ABSTRACT: We introduce a new synthetic concept that can be broadly adopted for the low-temperature preparation of mixed-metal energy storage materials, such as phosphates, silicates, fluorides, fluorophosphates, and fluorosulfates that exhibit intrinsic low electronic conductivity and thus require a carbon modulation. The development of novel low-temperature approaches for assembling energy-related materials with a complex core−shell microstructure is of great importance for expanding their application scope. The traditional definition of single-source precursors refers to their ability to yield a phase-pure material upon thermal decomposition. We have developed a new way for the utilization of heterometallic molecular precursors in synthesis that goes beyond its common delineation as a single-phase maker. The utility of this approach has been demonstrated upon the low-temperature synthesis of lithium-iron phosphate@C, which represents a celebrated cathode material for Li-ion batteries. The first atomically precise carbonaceous molecular precursors featuring a desired Li:Fe:P ratio of 1:1:1, divalent iron, and sufficient oxygen content for the target $LiFe^{II}PO4$ phosphate were shown to enable a spontaneous formation of both the olivine core and conductive carbon shell, yielding a carbon-coated mixed-metal phosphate.

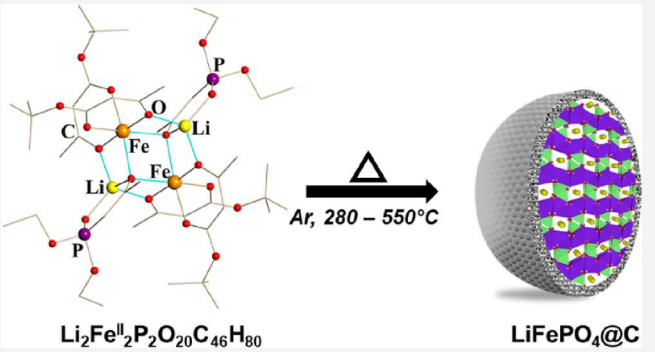

INTRODUCTION

Mixed-metal phosphates are known to be widely used as supercapacitors,[1] biofunctional materials,[2] cements,[3] electrolytes,[4] photocatalysts,[5] and dehydrogenation reagents[6] with high performance and low costs. However, the most important application of this class of compounds is cathode materials for rechargeable batteries.[7] The discovery of $LiFePO_4$ (LFP) has turned into an inspiring breakthrough in the exploration of electrochemically active materials for lithium-ion batteries (LIBs).[8−11] Being one of the most successfully commercialized LIB positive electrodes (cathodes), the olivine-type $LiFePO_4$ not only offers outstanding electrochemical properties but also highlights a large group of prospective mixed-metal phosphates with polyanion frameworks such as $LiFe_{0.6}Mn_{0.4}(PO)_4$,[12] $NaFePO_4$,[13] $Li_3V_2(PO_4)_3$,[14] $Na_3V_2(PO_4)_3$,[15] and $Li_2FeP_2O_7$[16] that allow for reversible Li(Na) ion (de)insertion while employing the abundant and ecologically friendly 3d transition metals.[17−19]

Materials that feature relatively complex chemical compositions commonly demand suitable or even specifically designed synthetic strategies to achieve expected compositional or morphological quality products. As for the mixed-metal phosphates, traditional preparation methods such as those of sol−gel, co-precipitation, hydrothermal, or solid-state synthesis have been broadly utilized.[20−23] While multi-source precursors (MSPs) have been extensively employed for the synthesis of these materials,[24] there are only a few reports on the utilization of single-source precursors (SSP). Phosphorylated ligands such as 1-hydroxy ethylidene-1,1-diphosphonate (HEDP),[25] hydrogenphosphate,[26] amino tris-(methylene phosphonate) (ATMP),[27] and phytic acid (PhyA)[28] have been explored while typically assisted by additional anionic groups (hydroxide and oxalate). Unfortunately, in all of these reports, the crystal structure and molecular nature of the precursor were not established with the proposed schematic models being highly questionable. The correct ratio of Li:M:P for the target material has not been confirmed, while clearly appearing wrong in some cases. Some of the methods require complicated synthetic procedures that certainly limit large-scale preparation.[27,28] In addition, the presence of trivalent iron in some of the precursors requires an extra pyrolytic reduction process (or co-ligand assistance)[29] that is unsafe when performed on a large scale. High decomposition temperatures (≥700 °C) to

Received: May 21, 2023
Published: July 28, 2023

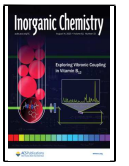

get the phase-pure phosphates upon calcination are somewhat contradictory with the advertised "soft chemistry" synthetic approach. Despite the above deficiencies, all these works clearly demonstrate the advantages of the SSP technique in the formation of phosphate cathode materials for high-power battery applications.

The most important advantages of mixed-metal phosphates as cathodes are their superior electrochemical reversibility and high operational safety, which derive from their intrinsically stable olivine structure.[9] Ironically, this same structure is also responsible for the low electronic conductivity due to the strong O sp^3−M 3d (M = transition metal) hybridization rendering compounds as Mott insulators.[30] The most effective way to address this issue is to employ a conductive carbon coating, which has been shown to greatly improve the specific capacity, cyclability, and rate performance of the Li/Na transition-metal phosphates.[31]

A number of methods have been suggested for the preparation of carbon-coated phosphate cathode materials.[10,31] Most of those are ex situ coating techniques that involve the thermal decomposition of organic precursors added to preformed phosphates. In particular, all of the abovementioned SSP reports were employing ex situ carbon sources (sucrose, glucose, and carbon matrix).[32−34] In contrast, the in situ coating approach refers to the carbon formation concomitant with the preparation of metal phosphates by thermolysis of a mixture of multiple precursors.[35,36] The carbon-coated composites obtained by the in situ technique generally exhibit superior electrochemical activity compared to those produced by the ex situ pathway.[37] This is primarily because the former coating procedure is capable of generating a tight-bound heterojunction interface between the carbon layer and material surface, which promotes better electron transfer between the two phases.[38]

Single-source precursors have long been established as "single-phase makers" by employing a molecule that incorporates all necessary elements in an appropriate ratio to yield the target material through mild-condition thermolysis. Traditionally, this approach specifically emphasizes the correct element type and ratio in the molecular precursor to ensure the phase-purity of the final product but overlooks its ability to spontaneously produce the specific multi-phase architectures.

In this work, we took the SSP approach one step further, namely, to design and isolate the first atomically precise molecular precursors, which can be used as an "all-in-one" entity in the preparation of composite mixed-metal phosphate/C nanocrystalline architectures. The inspiration for this research came from the investigation of Gedanken et al. who utilized[39−41] the decomposition of single-source precursors in an inert atmosphere to fabricate a carbon shell for the stabilized high-temperature metastable phases. The celebrated Li−Fe phosphate material has been selected as a target to illustrate the efficiency of our synthetic approach that can be applied to a great variety of Li/Na transition-metal phosphate materials. Herein, we present single-source precursors that bear the following important characteristics: (i) they represent well-defined and structurally characterized molecular compounds that feature three key elements, namely, Li, Fe, and P, mixed at the atomic level in a precise 1:1:1 ratio in order to ensure a highly homogeneous chemical distribution upon thermal decomposition; (ii) they contain divalent Fe as in the target material so that no exogenous reducing agents are required during the thermolysis; (iii) they have enough oxygen to form the desired phosphate in anoxic decomposition conditions needed to maintain the divalent oxidation state of iron; (iv) they exhibit both high volatility and solubility in common solvents to greatly expand the range of processing pathways, such as MOCVD or liquid injection methods, in order to obtain the carbon-coated composites in a variety of different forms; (v) they are prepared through a simple, one-pot synthesis using commercially/readily available reagents on a large scale with high yields and low processing costs in order to make it attractive for industrial applications; (vi) they yield phase-pure $LiFePO_4$ upon record-low decomposition temperatures; (vii) they feature carbonaceous ligands that are capable of in situ formation of carbon linkages between the $LiFePO_4$ nanoparticles.

RESULTS AND DISCUSSION

Design of Molecular Precursors. In order to design a heterometallic molecular precursor with a $Li:Fe^{II}:P$ ratio of 1:1:1, two major steps should be considered. First, one needs a model structure with the same number of lithium and transition metal ions. The latter should be divalent so that no exogenous reducing agents will be required to assist upon thermal decomposition of precursors. Despite an extensive synthetic efforts, only two model structure types with $Li:M^{II}$ = 1:1 (M = 3d transition metal) are currently available. One of those is polymeric chain $[LiML_3]_\infty$ that consists of alternating Li^+ and $[M^{II}L_3]^-$ units (Scheme 1a).[42] This structure tolerates ligands with only small substituents and is unlikely to accommodate any phosphorylated anions with bulky groups. In addition, all ligands are crystallographically equivalent making no clear preference for a specific mixed-ligand arrangement.

Scheme 1. Model structure types with Li:M ratio of 1:1

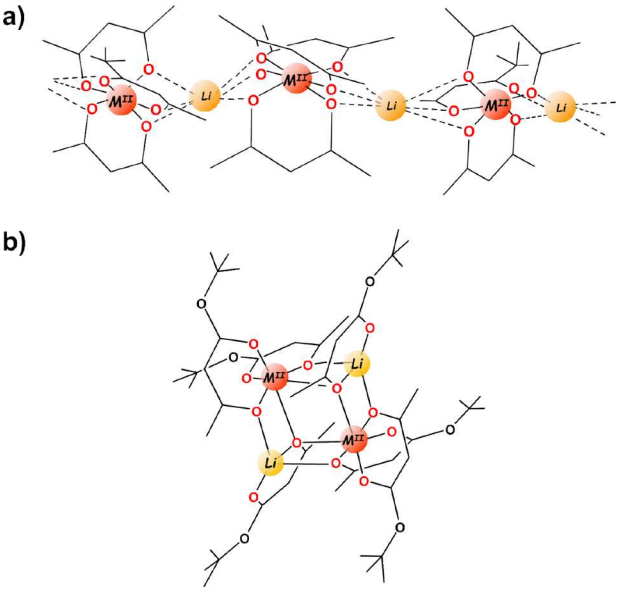

The other family of recently reported complexes, that is, $[Li_2M^{II}{}_2L_6]$ (Scheme 1b),[42−44] instantly appeared as the leading candidate. These compounds exhibit a cyclic tetranuclear structure and incorporate two Li and two divalent transition metal ions. The structure tolerates a number of primarily chelating ligands such as tbaoac (*tert*-butyl acetoacetate), dhd (2,2-dimethyl-hexanedionate), and ptac

https://doi.org/10.1021/acs.inorgchem.3c01664
Inorg. Chem. 2023, 62, 12931−12939

Scheme 2. Design of Heterometallic Tetranuclear Precursors with Li:Fe:P Ratio of 1:1:1

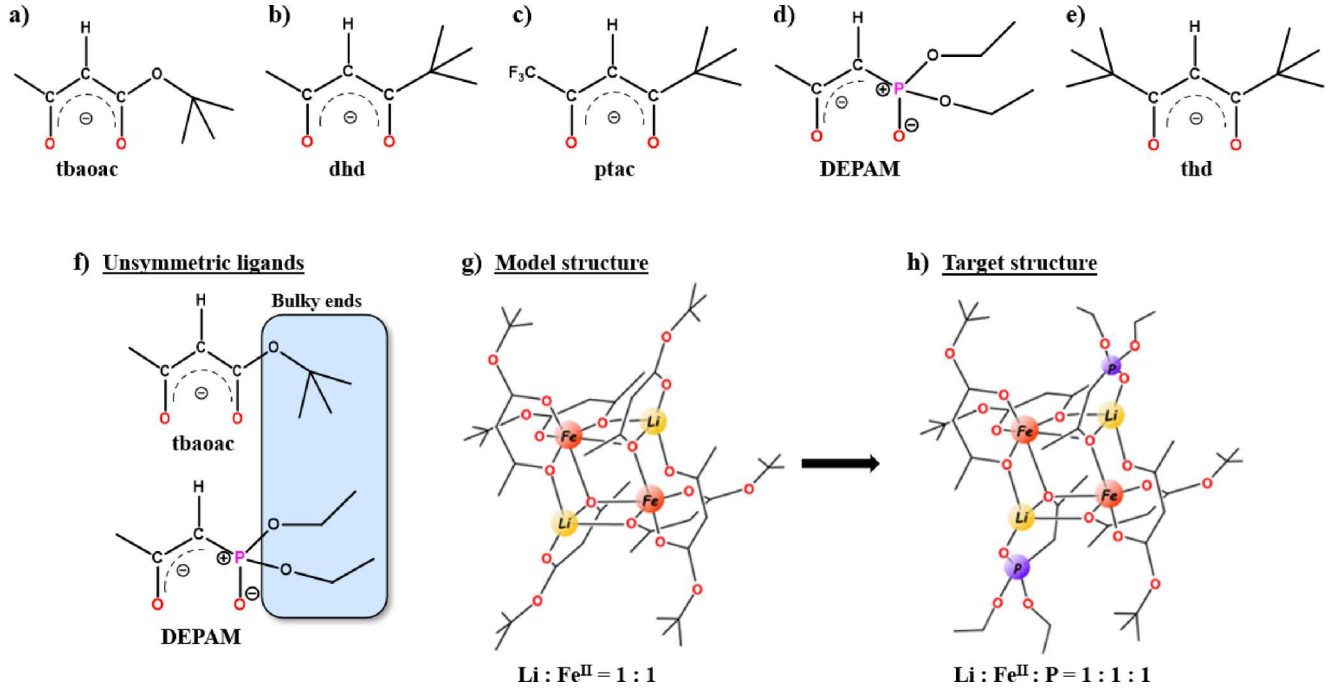

(1,1,1-trifluoro-5,5-dimethyl-2,4-hexanedionate) (Scheme 2a–c) that all have a common feature: they are unsymmetric (small/bulky). Importantly, there are two different types of ligands in this structure: four of those are primarily chelating transition-metal centers, while the other two coordinate with Li ions. Homoleptic compounds of $[Li_2M^{II}{}_2L_6]$ were found[42,43] to be soluble in a variety of common solvents and highly volatile and exhibit low decomposition temperatures as well as clean decomposition patterns.

The second step is the selection of an appropriate phosphorylated ligand that can be accommodated within the molecular structure. Upon thorough examination of a number of chelating/bridging ligands that contain a phosphorus atom, we chose the DEPAM (diethyl (2-oxopropyl)phosphate; Scheme 2d) group. This ligand is morphologically similar to unsymmetric (small/bulky) ligands (Scheme 2a–c) that support the tetranuclear molecular structure. The monoanionic DEPAM group that contains four oxygens per phosphorus atom bears a clear analogy with tbaoac (Scheme 2a) in polynuclear compounds of the type $[L_3M{-}M{-}ML_3]$ (M^{II} = Mg, Co, and Ni),[45,46] showing the same chelating/chelating–bridging coordination pattern for its two oxygens. What is even more important, DEPAM is expected to be a more electron-donating group compared to the ligands shown in Scheme 2a–c. As such, it should be anticipated to preferentially chelate the two Li centers, resulting in the $Li_2Fe_2(DEPAM)_2L_4$ (L = tbaoac, dhd, and ptac) composition with a Li:Fe^{II}:P ratio of 1:1:1 (Scheme 2f–h) needed for the precursor. In addition, the LiL (L = DEPAM, tbaoac, dhd, and ptac) salts that will be employed for the synthesis of heterometallic precursors are readily available.

Synthesis and Properties of Molecular Precursors. The single-source precursor approach inevitably requires an extra step in the preparation of the target material, which is the synthesis of the precursor itself. Therefore, in order to be competitive with other methods, the precursor synthesis should be carried out through a very simple and efficient one-pot procedure that does not contribute significantly to the cost of the final product.

Heterometallic, heteroleptic precursors $Li_2Fe_2(DEPAM)_2L_4$ (L = tbaoac (**1**), dhd (**2**), and ptac (**3**)) have been prepared via a one-step synthetic procedure by the interaction of commercial anhydrous iron(II) chloride with a mixture of readily available unsolvated lithium salts (eq 1). This reaction can be run in solution on a large scale with a nearly quantitative yield (see the Supporting Information for more information). The final heterometallic complex can be effectively separated from the LiCl byproduct based on different solubilities in non-/weakly coordinating solvents such as pentane or diethyl ether. Compounds **1**–**3** exhibit good solubility in a variety of common solvents, such as alcohols, acetone, diethyl ether, and pentane. In the solid state, they are relatively stable in the open air for a reasonable period of time but are very sensitive in solution, instantly turning into dark red upon contact with moist air, which is indicative of the formation of Fe^{3+} species. The precursors **1**–**3** are volatile and under dynamic vacuum (cold finger, 70 °C for **1** and 90 °C for **2** and **3**) they can be quantitatively collected in the cold zone of the container (see the Supporting Information for more information). The visual signs of the thermal decomposition can be clearly detected at approximately 100–110 °C in sealed, evacuated glass ampules.

$$2FeCl_2 + 2Li(DEPAM) + 4LiL \rightarrow Li_2Fe_2(DEPAM)_2L_4 + 4LiCl \quad (1)$$

Solid-State Structure of Molecular Precursors. X-ray single-crystal structure analysis confirmed that molecular precursors **1**–**3** exhibit a tetranuclear cyclic structure (Figure 1) with a divalent iron and Li:Fe:P ratio of 1:1:1. In all structures, two DEPAM ligands are located on the Li ions, while four tbaoac/dhd/ptac groups are chelating the Fe centers. All unsymmetric ligands act in the same fashion by providing their oxygens beneath the small methyl (trifluor-

https://doi.org/10.1021/acs.inorgchem.3c01664
Inorg. Chem. 2023, 62, 12931–12939

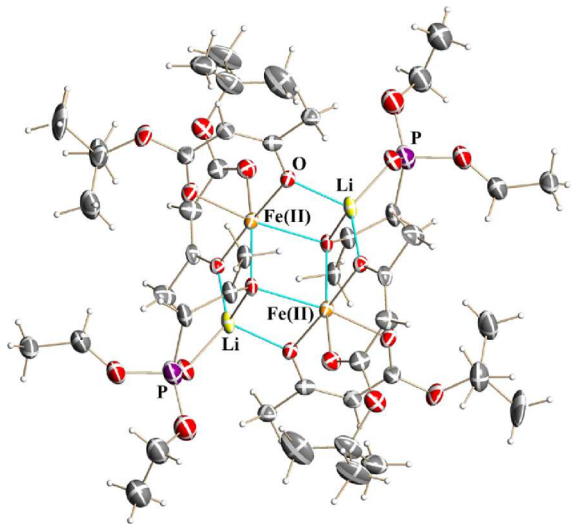

Figure 1. Solid-state structure of $[Li_2Fe^{II}_2(DEPAM)_2(tbaoac)_4]$ (**1**). Only Li, Fe, P, and O atoms are labeled. Hydrogen atoms are shown as balls with arbitrary radius. A full view of the molecular structures of **1**–**4** and bond distances and angles can be found in Figures S5–S11 and Tables S7–S13.

omethyl) substituents for bridging interactions that hold the heterometallic assembly together. On the other hand, the ligand oxygens proximal to the bulky substituents (O^tBu, ^tBu, and $(OEt)_2$) remain purely chelating (Figures S5–S10). It should be noted that no complexes with different ligand ratios or any isomers have been observed.

Interestingly, we were also able to involve the thd (2,2,6,6-tetramethyl-3,5-heptanedionate; Scheme 2e) ligand into the analogous structure of $[Li_2Fe_2(DEPAM)_2(thd)_4]$ (**4**) (see the Supporting Information for synthetic details). This symmetric ligand with two bulky ^{t}Bu groups on both ends is known[47] to act in a variety of coordination modes from pure chelating to bis-bridging (Figure S11 and Table S13). The acquisition of complex **4** clearly demonstrates the versatility of the model heterocyclic system to accommodate a variety of ligands. Inspection of the M–O distances in molecules **1**–**4** (Table 1)

Table 1. Averaged Metal–Oxygen Bond Distances (Å) in the Structures of Heterometallic Precursors 1–4 (the Full List of Bond Distances and Angles Can Be Found in Tables S7–S13)

L/M–O (Å)	Fe–O_c[a]	Fe–$O_{c\text{-}b}$[b]	Fe–O_b[c]	Li–O
tbaoac (**1**)[d]	2.131	2.039	2.165	1.926
dhd (**2**)	2.055	2.054	2.226	1.907
ptac (**3**)	2.059	2.059	2.185	1.940
thd (**4**)	2.038	2.081	2.167	1.952

[a]c: chelating. [b]c-b: chelating–bridging. [c]b: bridging. [d]Monoclinic polymorph.

confirms the similarities in their tetranuclear heterocyclic arrangement while displaying subtle differences associated with the ligand bulkiness as well as with molecular packing.

While four molecular precursors reported here feature similar structures as well as divalent Fe, they demonstrate different colors in solution (Figure 2a). Specifically, the complex **1** appears as green-yellow, **2** as yellow, **3** as orange, and **4** as deep violet. This could only be ascribed to the different ligands chelating with the Fe sites, which affect the metal–ligand transitions. Clearly, there is a trend that the absorption peaks are red-shifted along the sequence of tbaoac–thd–dhd–ptac groups (Figure 2a). Such an observation is well aligned with the electron-donating strength of the four anionic groups as the stronger electron-donating ligand should provide a wider energy gap for the HOMO–LUMO transition. The calculated HOMO–LUMO wavefunctions (Figure 2b) confirm the metal–ligand energy gap decreasing from **1** to **4** to **2** to **3**. Unfortunately, despite numerous attempts, we were unable to isolate the homoleptic complex $[Li_2Fe_2(DEPAM)_6]$ for the direct comparison of metal–ligand energy transitions.

Retention of the Heterometallic Structure in Solution and in the Gas Phase. One of the goals in designing a single-source precursor for lithium-iron phosphate was to make it suitable for a variety of techniques, such as CVD or liquid injection for the preparation of thin films and nanostructured materials. The key precursor characteristic for such applications is the retention of its heterometallic core whether in solution or in the gas phase. The ^{1}H and ^{7}Li NMR spectra of precursors in deuterated chloroform are silent (Figures S20 and S21), which suggests that the tetranuclear structure containing high-spin Fe^{II} ions remains intact. Dissociation of the heterometallic molecule into homometallic units in solutions of strongly coordinating solvents is accompanied by the instant appearance of the ^{7}Li and ^{1}H NMR signals for the lithium-containing fragments.

Mass spectrometric investigation of the solid samples (Figure 3) unambiguously revealed the presence of the heterometallic species upon evaporation of molecular precursors **1**–**4** (Figures S16–S19 and Tables S14–S24). For example, for compound **1**, the $[M\text{-tbaoac}]^+$ (M = $[Li_2Fe_2(DEPAM)_2(tbaoac)_4]$; meas/calcd = 983.2878/983.2876) and $[M\text{-DEPAM}]^+$ (meas/calcd = 977.2799/977.2793) ions can be clearly identified in the positive mode spectrum, showing excellent agreement with their respective calculated isotope distribution patterns.

Thermal Decomposition of Molecular Precursors. Molecular complexes **1**–**4** have been designed to act as single-source precursors to yield $LiFePO_4$ upon thermal decomposition. The use of suitable thermolysis conditions is critical to obtain the target decomposition product. Primarily, in order to keep the divalent Fe throughout the decomposition process, a strict anaerobic atmosphere is required. Indeed, our initial choice of air or oxygen environment to make $LiFePO_4$ phosphate was quickly shown to be wrong, instantly resulting in the oxidation of Fe^{2+} and the appearance of the Fe_2O_3/$Li_3Fe_2(PO_4)_3$ mixture in decomposition residues (Figure S22). Therefore, after numerous adjustments, we turned to a combination of an argon/vacuum atmosphere for pyrolysis. Phase-pure $LiFePO_4$ can be obtained by the thermal decomposition of single-source precursors **1** and **2** (Figures S23–26 and S28 and Tables S25 and S26). Thermolysis of complexes **3** and **4** resulted in an appearance of minor impurities of Li_3PO_4 (Figures S29 and S30 and Tables S27 and S28) no matter which conditions have been applied.

Out of four prospective single-source precursors, $[Li_2Fe_2(DEPAM)_2(tbaoac)_4]$ (**1**) exhibits the lowest decomposition temperature of 280 °C to the target phosphate (Figure S23 and S31–33). Increasing the annealing temperature for precursor **1** leads to improved crystallinity of the product (SI, Figures S24–26). The unique low-temperature decomposition pattern of molecular precursor **1** could be attributed to the employment of the tbaoac group, which is in

https://doi.org/10.1021/acs.inorgchem.3c01664
Inorg. Chem. 2023, 62, 12931–12939

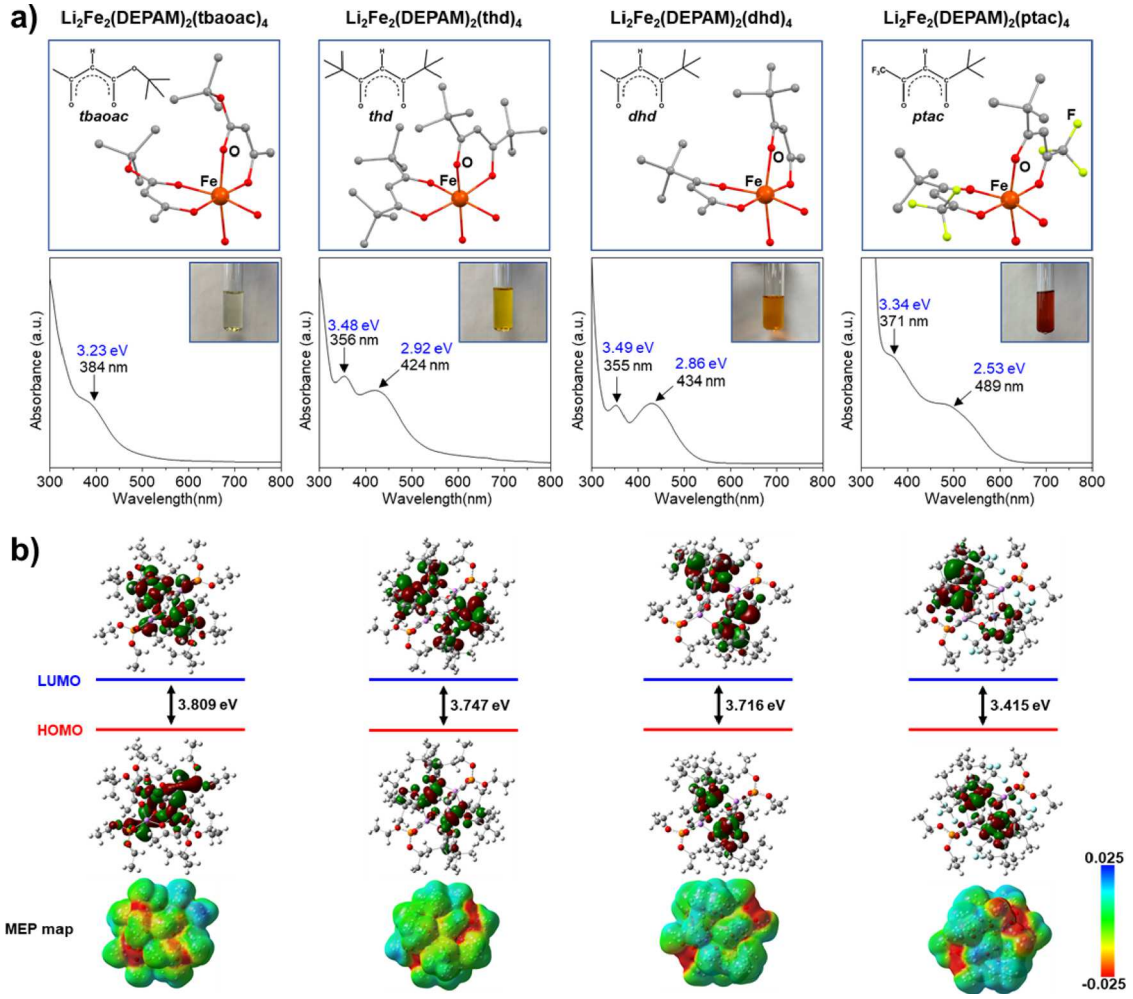

Figure 2. (a) Absorption spectra and solution colors of molecular precursors **1**, **4**, **2**, and **3** (from left to right). The electronic structures for the molecular assembly $[Li_2Fe_2(DEPAM)_2L_4]$ are effectively influenced by the ligands (L) chelating with the Fe ions. (b) HOMO and LUMO orbitals (top) and the molecular electrostatic potential (MEP) maps for the molecular precursors **1**, **4**, **2**, and **3** (bottom).

line with our previous observations[43] of this ligand behavior. In addition, the complex **1** is also advantageous with respect to the preparation, volatility, and, especially, low cost. For molecular precursor **1**, the ligand contributions to the cost of the target phosphate material are estimated as 2.4 and 0.8% for DEPAM and tbaoac, respectively, which are miniscule compared to those in **2**–**4** (Table 2). Most importantly, the thermal decomposition of precursor **1** was found to result in the appearance of the conductive carbon among the target residue (Figure 4a). Therefore, further investigation has been focused on the utilization of **1** as a single-source precursor for the $LiFePO_4$/C material.

Thermogravimetric (TGA) study of heterometallic precursor **1** under Ar confirmed that the decomposition starts at around 110 °C (Figure S34a). The isotherm curve measured for the sample pre-heated at 200 °C under an argon atmosphere for 2 h shows that the weight loss is largely over at 280 °C after 6 h (Figure S34b). X-ray powder diffraction analysis of decomposition residues revealed that single-source precursor $[Li_2Fe_2(DEPAM)_2(tbaoac)_4]$ (**1**) yields crystalline phase-pure $LiFePO_4$ in the temperature range of 280–550 °C under argon/vacuum conditions (Figure 4b). Thermolysis below 280 °C as well as upon increasing the annealing temperature to 600 °C results in the appearance of unidentified peaks in the decomposition residues (Figure S27).

The phase-pure material with the olivine-type *Pnma* structure was verified for the 280–550 °C thermal decomposition products according to the Rietveld refinement (Figures S23–S26) of X-ray powder diffraction patterns. The unit cell volume of the residues obtained at higher temperatures is slightly lower than for the 280 °C pyrolysis product (Table S25), indicating a growing particle size. High-angle annular dark field scanning TEM (HAADF-STEM) images confirm the coarsening of the $LiFePO_4$ particles up to 50–100 nm, whereas ED patterns and high-resolution transmission electron microscopy (HRTEM) images reflect their high crystallinity and intimate mixing with carbon, as shown by compositional energy-dispersive X-ray (EDX) mapping in the scanning TEM mode (Figure 4c). Quantitative EDX analysis reveals a stoichiometric (1.01(2):0.99(2)) and highly homogeneous distribution of Fe and P (Figure 4d). The carbon content in the samples of $LiFePO_4$@C materials was found to decrease upon increasing the decomposition temperature. While it is relatively high in the 280 °C sample (approximately 20 wt %), it drops down to 9.8 and 5.5% for the 500 and 550 °C samples, respectively.

https://doi.org/10.1021/acs.inorgchem.3c01664
Inorg. Chem. 2023, 62, 12931−12939

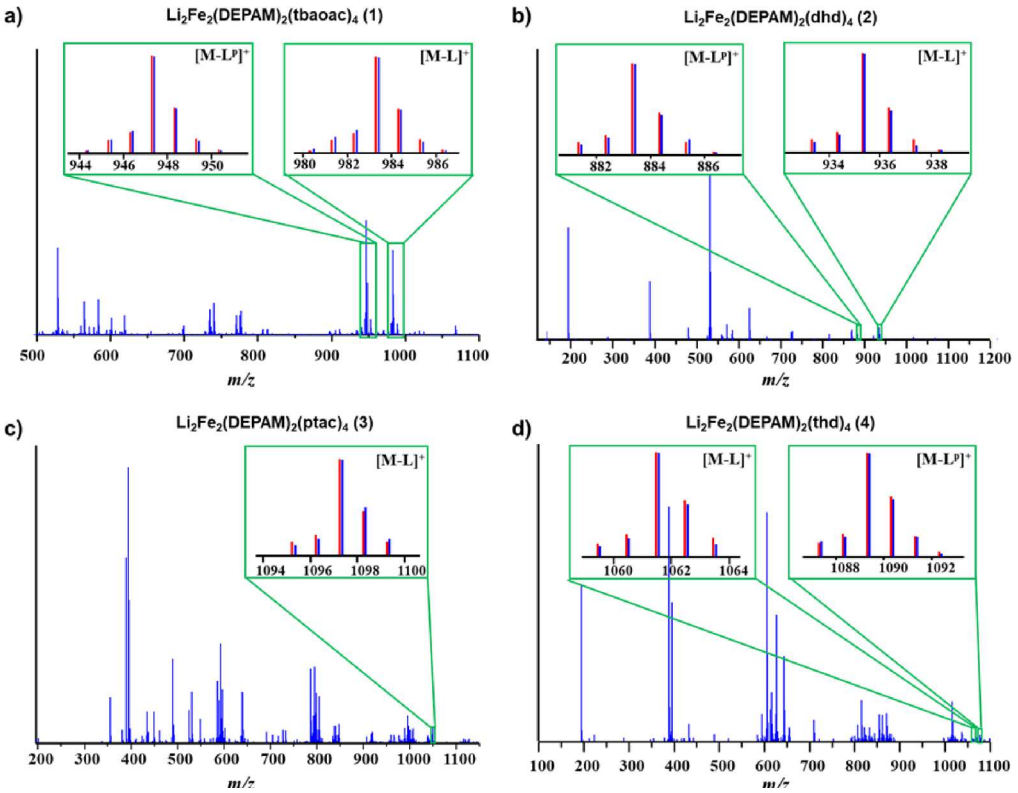

Figure 3. Positive ion DART mass spectra of solid compounds **1**−**4**. The isotope distribution patterns for the $[M - L]^+$ and $[M - L^P]^+$ (M = $Li_2Fe_2(DEPAM)_2L_4$, L^P = DEPAM, L = tbaoac, dhd, ptac, and thd) ions are shown in the insets.

Table 2. Properties of Heterometallic Precursors $[Li_2Fe_2(DEPAM)_2L_4]$ (L = tbaoac (1), dhd (2), ptac (3), and thd (4))

	L			
property	tbaoac (**1**)	dhd (**2**)	ptac (**3**)	thd (**4**)
yield	96%	92%	93%	96%
volatility[a]	70 °C[a]	90 °C	90 °C	90 °C
decomposition (visual signs)	100 °C	110 °C	110 °C	110 °C
lowest temperature to yield $LiFePO_4$	280 °C	500 °C	500 °C[b]	500 °C[b]
ligand cost contribution (%)[c]	0.8%	43.9%	25.3%	17.3%

[a]Dynamic vacuum conditions. [b]Impurities were detected. [c]To produce 1 mole of $LiFePO_4$.

The near-surface structure of the carbon coating on $LiFePO_4$ was analyzed by Raman spectroscopy (Figure 4e) as carbon is a relatively strong scatterer with two E_{2g} modes.[48] For pure $LiFePO_4$ without any carbon coating, there are two characteristic sharp bands at approximately 950 and 1095 cm^{-1}, corresponding to the symmetric A_g (ν_1) and asymmetric (ν_3) $(PO_4)^{3-}$ stretching modes.[49] When carbon is coating the surface of $LiFePO_4$, these two peaks are attenuated since much of the laser beam is scattered by carbon. Two intense bands at approximately 1348 and 1608 cm^{-1} correspond to the Raman scattering from the disordered (D) and graphite (G) carbon phases.[50] The Raman spectrum of the $LiFePO_4$@C obtained after decomposition at 280 °C displays relatively strong characteristic peaks for $(PO_4)^{3-}$, while both graphite and disordered carbon stretches are weak (Figure S35), indicating that, though the $LiFePO_4$ core has been formed at such a low temperature, the incompletely decomposed organic residues are still present as carbohydrates. Starting with a 350 °C sample, the $(PO_4)^{3-}$ stretching peaks are obviously weakened, suggesting the formation of an elemental carbon coating layer on the surface of the preformed $LiFePO_4$. One can observe a clear trend that the graphite/disordered (G/D) carbon ratio grows upon increasing the decomposition temperature, which is roughly estimated as 0.9, 1.2, and 1.4 for the products obtained by thermolysis of the precursor at 350, 500, and 550 °C, respectively (Figure 4e).

While we did not perform a full optimization of decomposition conditions in this work, we selected the $LiFePO_4$@C sample obtained from precursor **1** at 550 °C for electrochemical study. The product is phase-pure and has the lowest carbon content and highest G/D carbon ratio, and, importantly, it does not show any loss of Li upon thermal decomposition with the Li:Fe:P ratio found to be 0.984:1:0.957 by the ICP-OES technique. Cyclic voltammetry (CV) analysis was conducted at a scanning rate of 5 mV/s (Figure S36a). The obvious oxidation (3.6 V) and reduction (3.3 V) peaks correspond to the lithium ion extraction and insertion from/to the olivine structure, respectively, which aligns well with the commonly reported CV behavior for $LiFePO_4$.

The galvanostatic profiles at different rates indicate that $LiFePO_4$@C obtained under such conditions exhibits an overall good reversible capacity. At a relatively low cycling rate of 0.2 C, the maximum capacity can reach 162 mAh/g (theoretical capacity is 170 mAh/g) with a Coulombic efficiency of approximately 97%. At higher charge−discharge rates of 0.5, 1, and 2 C, the sample still maintains reasonable discharge capacities of 150, 140, and 118 mAh/g, respectively (Figure S36b). In addition, the reversibility of the as-prepared

https://doi.org/10.1021/acs.inorgchem.3c01664
Inorg. Chem. 2023, 62, 12931−12939

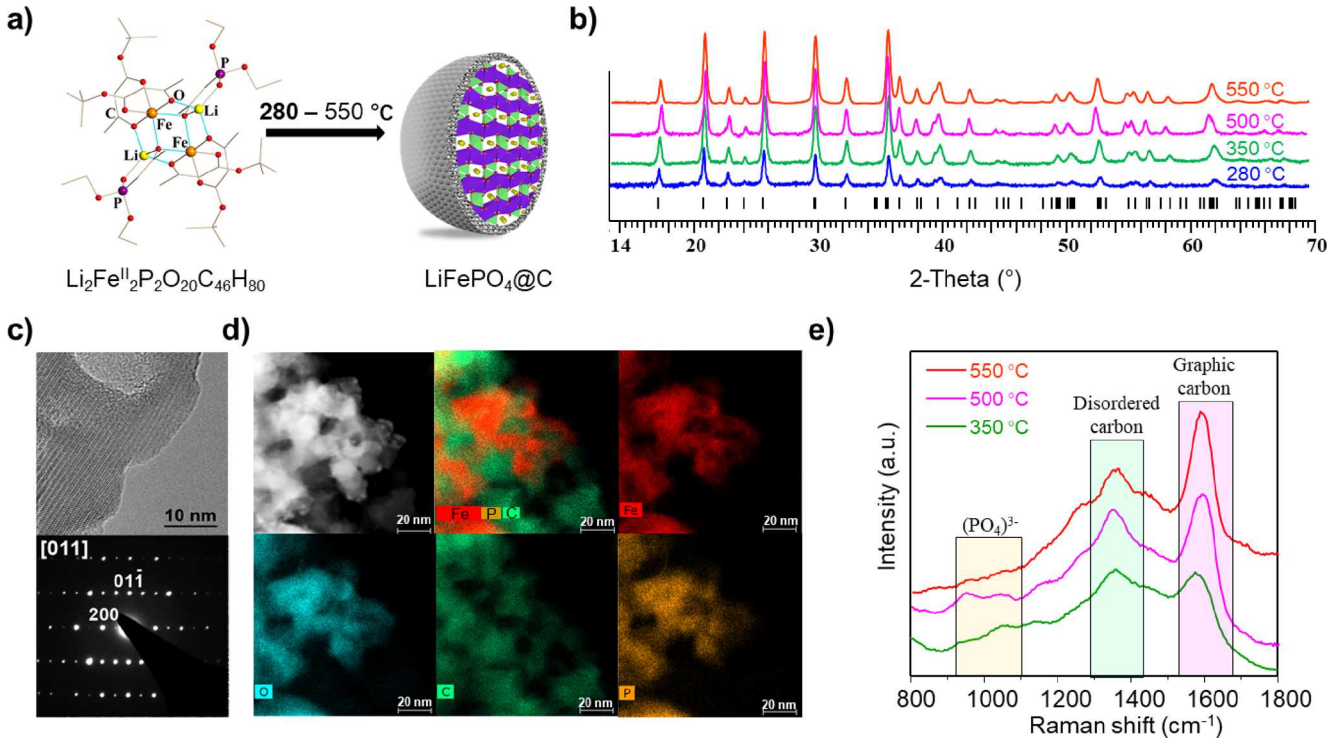

Figure 4. (a) Schematic representation of the preparation of the $LiFePO_4$@C composite material by thermal decomposition of single-source precursor **1**. (b) X-ray powder diffraction patterns of $LiFePO_4$ obtained by thermal decomposition of molecular precursor **1** at the temperatures of 280 (blue), 350 (green), 500 (purple), and 550 °C (orange) in the argon/vacuum atmosphere. Theoretical peak positions are shown at the bottom. Rietveld refinement for all samples can be found in Figures S23–S26 and Table S25. (c) HRTEM image and ED pattern of the nanoparticles obtained by thermal decomposition of precursor **1** at 500 °C. The ED pattern was indexed with the *Pnma* space group. (d) HAADF-STEM image (top left) of the $LiFePO_4$@C product along with the compositional EDX maps for Fe, O, C, and P and the color-coded mixed Fe/P/C map. (e) Raman spectra of the $LiFePO_4$@C material obtained by thermal decomposition of precursor **1** at 350 (green), 500 (purple), and 550 °C (orange) in the argon/vacuum atmosphere.

cathode material was also tested at a rate of 0.2 C, displaying good capacity retention of approximately 93.8% after 200 cycles (Figure S36c). The overall electrochemical performance of our $LiFePO_4$@C composite is comparable to the materials obtained by other techniques.[51,52] For the first time, the $LiFePO_4$@C material has been obtained from a single-source precursor, which is a well-characterized molecule containing Li, Fe, P, O, and C. This confirms that the suggested approach works well, while the electrochemical characteristics of the cathode material could be further improved by thorough optimization of decomposition conditions.

CONCLUSIONS

We introduce here a new synthetic concept of single-source precursor utilization that goes beyond its common definition as a single-phase maker. To the best of our knowledge, this study is the first to show that a complex carbon-coated architecture can be effectively obtained upon thermal decomposition of a structurally well-defined heterometallic molecular system.

We report a cheap and easy-to-make single-source precursor that produces the carbon-coated mixed-metal phosphate in a single step at relatively low temperatures. Importantly, the synthetic approach described in this work can be broadly adopted for the low-temperature preparation of not only phosphates but also for other classes of complex functional materials, such as fluorides, silicates, fluorophosphates, and fluorosulfates that are known to exhibit intrinsic low electronic conductivity and thus require carbon modulation.

ASSOCIATED CONTENT

Supporting Information

The Supporting Information is available free of charge at https://pubs.acs.org/doi/10.1021/acs.inorgchem.3c01664.

Experimental procedures, powder X-ray diffraction patterns of precursors, X-ray crystallographic procedures, NMR, IR, and DART-MS spectra, thermal gravimetric analysis, powder X-ray diffraction patterns of target materials, Raman spectra, electron microscopy, and electrochemical investigation of thermal decomposition products (PDF)

Accession Codes

CCDC 2029281, 2175198, and 2242625–2242627 contain the supplementary crystallographic data for this paper. These data can be obtained free of charge via www.ccdc.cam.ac.uk/data_request/cif, or by emailing data_request@ccdc.cam.ac.uk, or by contacting The Cambridge Crystallographic Data Centre, 12 Union Road, Cambridge CB2 1EZ, UK; fax: +44 1223 336033.

AUTHOR INFORMATION

Corresponding Author

Evgeny V. Dikarev – *Department of Chemistry, University at Albany, Albany, New York 12222, United States;* orcid.org/0000-0001-8979-7914; Email: edikarev@albany.edu

https://doi.org/10.1021/acs.inorgchem.3c01664
Inorg. Chem. 2023, 62, 12931–12939

Authors

Haixiang Han − *Department of Chemistry, University at Albany, Albany, New York 12222, United States; School of Materials Science and Engineering, Tongji University, Shanghai 201804, China;* orcid.org/0000-0002-8465-9624

Yuxuan Zhang − *Department of Chemistry, University at Albany, Albany, New York 12222, United States*

Zheng Zhou − *Department of Chemistry, University at Albany, Albany, New York 12222, United States; School of Materials Science and Engineering, Tongji University, Shanghai 201804, China*

Jesse C. Carozza − *Department of Chemistry, University at Albany, Albany, New York 12222, United States*

Zheng Wei − *Department of Chemistry, University at Albany, Albany, New York 12222, United States*

Alexander S. Filatov − *Department of Chemistry, The University of Chicago, Chicago, Illinois 60637, United States;* orcid.org/0000-0002-8378-1994

Andrey Shevtsov − *Skolkovo Institute of Science and Technology, Moscow 143026, Russia*

Artem M. Abakumov − *Skolkovo Institute of Science and Technology, Moscow 143026, Russia;* orcid.org/0000-0002-7135-4629

Complete contact information is available at: https://pubs.acs.org/10.1021/acs.inorgchem.3c01664

Notes

The authors declare no competing financial interest.

Dedicated to the memory of Dr. Carlos A. Murillo, scientist, educator, mentor, and friend.

■ ACKNOWLEDGMENTS

Financial support from the National Science Foundation is gratefully acknowledged (no. CHE-1955585). NSF's ChemMatCARS, Sector 15 at the Advanced Photon Source (APS), Argonne National Laboratory (ANL) is supported by the Divisions of Chemistry (CHE) and Materials Research (DMR), National Science Foundation, under grant no. NSF/CHE- 1834750. This research used resources of the Advanced Photon Source, a U.S. Department of Energy (DOE) Office of Science user facility operated for the DOE Office of Science by Argonne National Laboratory under contract no. DE-AC02-06CH11357.

■ REFERENCES

(1) Li, X.; Xiao, X.; Li, Q.; Wei, J.; Xue, H.; Pang, H. Metal (M = Co, Ni) Phosphate Based Materials for High-Performance Supercapacitors. *Inorg. Chem. Front.* **2018**, *5*, 11−28.

(2) Abou Neel, E. A.; Pickup, D. M.; Valappil, S. P.; Newport, R. J.; Knowles, J. C. Bioactive Functional Materials: A Perspective on Phosphate-Based Glasses. *J. Mater. Chem.* **2009**, *19*, 690−701.

(3) Chau, C. K.; Qiao, F.; Li, Z. Microstructure of Magnesium Potassium Phosphate Cement. *Constr. Build. Mater.* **2011**, *25*, 2911−2917.

(4) Wu, N.; Chien, P.-H.; Li, Y.; Dolocan, A.; Xu, H.; Xu, B.; Grundish, N. S.; Jin, H.; Hu, Y.-Y.; Goodenough, J. B. Fast Li+ Conduction Mechanism and Interfacial Chemistry of a NASICON/Polymer Composite Electrolyte. *J. Am. Chem. Soc.* **2020**, *142*, 2497−2505.

(5) Martin, D. J.; Liu, G.; Moniz, S. J. A.; Bi, Y.; Beale, A. M.; Ye, J.; Tang, J. Efficient Visible Driven Photocatalyst, Silver Phosphate: Performance, Understanding and Perspective. *Chem. Soc. Rev.* **2015**, *44*, 7808−7828.

(6) Bautista, F. M.; Campelo, J. M.; Luna, D.; Marinas, J. M.; Quirós, R. A.; Romero, A. A. Screening of Amorphous Metal−Phosphate Catalysts for the Oxidative Dehydrogenation of Ethylbenzene to Styrene. *Appl. Catal., B* **2007**, *70*, 611−620.

(7) Ling, J.; Karuppiah, C.; Krishnan, S. G.; Reddy, M. V.; Misnon, I. I.; Ab Rahim, M. H.; Yang, C.-C.; Jose, R. Phosphate Polyanion Materials as High-Voltage Lithium-Ion Battery Cathode: A Review. *Energy Fuels* **2021**, *35*, 10428−10450.

(8) Padhi, A. K.; Nanjundaswamy, K. S.; Goodenough, J. B. Phospho-olivines as Positive-Electrode Materials for Rechargeable Lithium Batteries. *J. Electrochem. Soc.* **1997**, *144*, 1188−1194.

(9) Sun, C.; Rajasekhara, S.; Goodenough, J. B.; Zhou, F. Monodisperse Porous $LiFePO_4$ Microspheres for a High Power Li-Ion Battery Cathode. *J. Am. Chem. Soc.* **2011**, *133*, 2132−2135.

(10) Zhang, W.-J. Structure and Performance of $LiFePO_4$ Cathode Materials: A Review. *J. Power Sources* **2011**, *196*, 2962−2970.

(11) Eftekhari, A. $LiFePO_4$/C Nanocomposites for Lithium-Ion Batteries. *J. Power Sources* **2017**, *343*, 395−411.

(12) Mi, Y.; Gao, P.; Liu, W.; Zhang, W.; Zhou, H. Carbon Nanotube-Loaded Mesoporous LiFe0.6Mn0.4PO4/C Microspheres as High Performance Cathodes for Lithium-Ion Batteries. *J. Power Sources* **2014**, *267*, 459−468.

(13) Oh, S.-M.; Myung, S.-T.; Hassoun, J.; Scrosati, B.; Sun, Y.-K. Reversible $NaFePO_4$ Electrode for Sodium Secondary Batteries. *Electrochem. Commun.* **2012**, *22*, 149−152.

(14) Rui, X.; Yan, Q.; Skyllas-Kazacos, M.; Lim, T.-M. $Li_3V_2(PO_4)_3$ Cathode Materials for Lithium-Ion Batteries: A Review. *J. Power Sources* **2014**, *258*, 19−38.

(15) Jian, Z.; Zhao, L.; Pan, H.; Hu, Y.-S.; Li, H.; Chen, W.; Chen, L. Carbon Coated $Na_3V_2(PO_4)_3$ as Novel Electrode Material for Sodium Ion Batteries. *Electrochem. Commun.* **2012**, *14*, 86−89.

(16) Clark, J.-M.; Nishimura, S.-I.; Yamada, A.; Islam, M.-S. High-Voltage Pyrophosphate Cathode: Insights into Local Structure and Lithium-Diffusion Pathways. *Am. Ethnol.* **2012**, *124*, 13326−13330.

(17) Masquelier, C.; Croguennec, L. Polyanionic (Phosphates, Silicates, Sulfates) Frameworks as Electrode Materials for Rechargeable Li (or Na) Batteries. *Chem. Rev.* **2013**, *113*, 6552−6591.

(18) Kim, H.; Park, I.; Seo, D.-H.; Lee, S.; Kim, S.-W.; Kwon, W. J.; Park, Y.-U.; Kim, C. S.; Jeon, S.; Kang, K. New Iron-Based Mixed-Polyanion Cathodes for Lithium and Sodium Rechargeable Batteries: Combined First Principles Calculations and Experimental Study. *J. Am. Chem. Soc.* **2012**, *134*, 10369−10372.

(19) Li, Z.; Zhang, D.; Yang, F. Developments of Lithium-Ion Batteries and Challenges of $LiFePO_4$ as One Promising Cathode Material. *J. Mater. Sci.* **2009**, *44*, 2435−2443.

(20) Yang, M.-R.; Ke, W.-H.; Wu, S.-H. Preparation of $LiFePO_4$ Powders by Co-Precipitation. *J. Power Sources* **2005**, *146*, 539−543.

(21) Lee, S. B.; Jang, I. C.; Lim, H. H.; Aravindan, V.; Kim, H. S.; Lee, Y. S. Preparation and Electrochemical Characterization of $LiFePO_4$ Nanoparticles with High Rate Capability by a Sol−Gel Method. *J. Alloys Compd.* **2010**, *491*, 668−672.

(22) Meligrana, G.; Gerbaldi, C.; Tuel, A.; Bodoardo, S.; Penazzi, N. Hydrothermal Synthesis of High Surface $LiFePO_4$ Powders as Cathode for Li-Ion Cells. *J. Power Sources* **2006**, *160*, 516−522.

(23) Wang, Y.; Feng, Z.-S.; Chen, J.-J.; Zhang, C. Synthesis and Electrochemical Performance of $LiFePO_4$/Graphene Composites by Solid-State Reaction. *Mater. Lett.* **2012**, *71*, 54−56.

(24) Li, X.; Shao, Z.; Liu, K.; Zhao, Q.; Liu, G.; Xu, B. Influence of Synthesis Method on the Performance of the $LiFePO_4$/C Cathode Material. *Colloids Surf., A* **2017**, *529*, 850−855.

(25) Wang, B.; Qiu, Y.; Yang, L. Structural and Electrochemical Characterization of $LiFePO_4$ Synthesized by an HEDP-Based Soft-Chemistry Route. *Electrochem. Commun.* **2006**, *8*, 1801−1805.

(26) Hameed, A. S.; Reddy, M. V.; Chowdari, B. V. R.; Vittal, J. J. Carbon Coated $Li_3V_2(PO_4)_3$ from the Single-Source Precursor, $Li_2(VO)_2(HPO_4)_2(C_2O_4)\cdot 6H_2O$ as Cathode and Anode Materials for Lithium Ion Batteries. *Electrochim. Acta* **2014**, *128*, 184−191.

(27) Chen, M.; Shao, L.-L.; Yang, H.-B.; Zhao, Q.-Y.; Yuan, Z.-Y. Organophosphonic Acid as Precursor to Prepare $LiFePO_4$/Carbon

Nanocomposites for High-Power Lithium Ion Batteries. *Electrochim. Acta* **2015**, *168*, 59−68.
(28) Zhao, Q.; Zhang, Y.; Meng, Y.; Wang, Y.; Ou, J.; Guo, Y.; Xiao, D. Phytic Acid Derived $LiFePO_4$ beyond Theoretical Capacity as High-Energy Density Cathode for Lithium Ion Battery. *Nano Energy* **2017**, *34*, 408−420.
(29) Jugović, D.; Uskoković, D. A Review of Recent Developments in the Synthesis Procedures of Lithium Iron Phosphate Powders. *J. Power Sources* **2009**, *190*, 538−544.
(30) Yang, J.; Wang, J.; Tang, Y.; Wang, D.; Li, X.; Hu, Y.; Li, R.; Liang, G.; Sham, T.-K.; Sun, X. $LiFePO_4$−Graphene as a Superior Cathode Material for Rechargeable Lithium Batteries: Impact of Stacked Graphene and Unfolded Graphene. *Energy Environ. Sci.* **2013**, *6*, 1521.
(31) Wang, J.; Sun, X. Understanding and Recent Development of Carbon Coating on $LiFePO_4$ cathode Materials for Lithium-Ion Batteries. *Energy Environ. Sci.* **2012**, *5*, 5163−5185.
(32) Wang, K.; Cai, R.; Yuan, T.; Yu, X.; Ran, R.; Shao, Z. Process Investigation, Electrochemical Characterization and Optimization of $LiFePO_4$/C Composite from Mechanical Activation Using Sucrose as Carbon Source. *Electrochim. Acta* **2009**, *54*, 2861−2868.
(33) Wang, L.; Liang, G. C.; Ou, X. Q.; Zhi, X. K.; Zhang, J. P.; Cui, J. Y. Effect of Synthesis Temperature on the Properties of $LiFePO_4$/C Composites Prepared by Carbothermal Reduction. *J. Power Sources* **2009**, *189*, 423−428.
(34) Wang, G.; Liu, H.; Liu, J.; Qiao, S.; Lu, G. M.; Munroe, P.; Ahn, H. Mesoporous $LiFePO_4$/C Nanocomposite Cathode Materials for High Power Lithium Ion Batteries with Superior Performance. *Adv. Mater.* **2010**, *22*, 4944−4948.
(35) Mi, C. H.; Cao, G. S.; Zhao, X. B. Low-Cost, One-Step Process for Synthesis of Carbon-Coated $LiFePO_4$ Cathode. *Mater. Lett.* **2005**, *59*, 127−130.
(36) Gong, H.; Xue, H.; Wang, T.; He, J. In-Situ Synthesis of Monodisperse Micro-Nanospherical $LiFePO_4$ /Carbon Cathode Composites for Lithium-Ion Batteries. *J. Power Sources* **2016**, *318*, 220−227.
(37) Doeff, M. M.; Wilcox, J. D.; Kostecki, R.; Lau, G. Optimization of Carbon Coatings on $LiFePO_4$. *J. Power Sources* **2006**, *163*, 180−184.
(38) Wang, J.; Yang, J.; Tang, Y.; Liu, J.; Zhang, Y.; Liang, G.; Gauthier, M.; Karen Chen-Wiegart, Y.-C.; Norouzi Banis, M.; Li, X.; Li, R.; Wang, J.; Sham, T. K.; Sun, X. Size-Dependent Surface Phase Change of Lithium Iron Phosphate during Carbon Coating. *Nat. Commun.* **2014**, *5*, 3415.
(39) Pol, S. V.; Pol, V. G.; Seisenbaeva, G.; Kessler, V. G.; Gedanken, A. Stabilization of Metastable Face-Centered Cubic Cobalt and the Tetragonal Phase of Zirconia by a Carbon Shell: Reaction under Autogenic Pressure at Elevated Temperature of $CoZr_2(acac)_2(O^iPr)_8$. *Chem. Mater.* **2004**, *16*, 1793−1798.
(40) Pol, S. V.; Pol, V. G.; Gedanken, A.; Spijksma, G. I.; Grinblat, J.; Selvan, R. K.; Kessler, V. G.; Seisenbaeva, G. A.; Gohil, S. Synthesis of Nanocrystalline Zirconium Titanate and Its Dielectric Properties. *J. Phys. Chem. C* **2007**, *111*, 2484−2489.
(41) Pol, V. G.; Pol, S. V.; Gedanken, A.; Kessler, V. G.; Seisenbaeva, G. A.; Sung, M.-G.; Asai, S. Applied Magnetic Field Rejects the Coating of Ferromagnetic Carbon from the Surface of Ferromagnetic Cobalt: RAPET of $CoZr_2$ $(acac)_2(O^iPr)_8$. *J. Phys. Chem. B* **2005**, *109*, 6121−6125.
(42) Han, H.; Wei, Z.; Barry, M. C.; Filatov, A. S.; Dikarev, E. V. Heterometallic Molecular Precursors for a Lithium−Iron Oxide Material: Synthesis, Solid State Structure, Solution and Gas-Phase Behaviour, and Thermal Decomposition. *Dalton Trans.* **2017**, *46*, 5644−5649.
(43) Wei, Z.; Han, H.; Filatov, A. S.; Dikarev, E. V. Changing the Bridging Connectivity Pattern within a Heterometallic Assembly: Design of Single-Source Precursors with Discrete Molecular Structures. *Chem. Sci.* **2014**, *5*, 813−818.
(44) Han, H.; Wei, Z.; Barry, M. C.; Carozza, J. C.; Alkan, M.; Rogachev, A. Y.; Filatov, A. S.; Abakumov, A. M.; Dikarev, E. V. A Three Body Problem: A Genuine Heterotrimetallic Molecule vs. a Mixture of Two Parent Heterobimetallic Molecules. *Chem. Sci.* **2018**, *9*, 4736−4745.
(45) Cotton, F. A.; Schunn, R. A. Metal Salts and Complexes of Dialkoxyphosphonylacetylmethanide Ions. *J. Am. Chem. Soc.* **1963**, *85*, 2394−2402.
(46) Cotton, F. A.; Huegel, R.; Eiss, R. Molecular Structure of a Trinuclear Cobalt(II) Complex of the Diethoxyphosphonylacetylmethane Anion. *Inorg. Chem.* **1968**, *7*, 18−23.
(47) Eisentraut, K. J.; Sievers, R. E. Volatile Rare Earth Chelates. *J. Am. Chem. Soc.* **1965**, *87*, 5254−5256.
(48) Wu, J.; Dathar, G. K. P.; Sun, C.; Theivanayagam, M. G.; Applestone, D.; Dylla, A. G.; Manthiram, A.; Henkelman, G.; Goodenough, J. B.; Stevenson, K. J. *In Situ* Raman Spectroscopy of $LiFePO_4$: Size and Morphology Dependence during Charge and Self-Discharge. *Nanotechnology* **2013**, *24*, 424009.
(49) Bai, Y.; Yin, Y.; Yang, J.; Qing, C.; Zhang, W. Raman Study of Pure, C-Coated and Co-Doped $LiFePO_4$: Thermal Effect and Phase Stability upon Laser Heating. *J. Raman Spectrosc.* **2011**, *42*, 831−838.
(50) Vu, A.; Stein, A. Multiconstituent Synthesis of $LiFePO_4$/C Composites with Hierarchical Porosity as Cathode Materials for Lithium Ion Batteries. *Chem. Mater.* **2011**, *23*, 3237−3245.
(51) Wang, S.; Yang, H.; Feng, L.; Sun, S.; Guo, J.; Yang, Y.; Wei, H. A Simple and Inexpensive Synthesis Route for $LiFePO_4$/C Nanoparticles by Co-Precipitation. *J. Power Sources* **2013**, *233*, 43−46.
(52) Murugan, A. V.; Muraliganth, T.; Manthiram, A. Comparison of Microwave Assisted Solvothermal and Hydrothermal Syntheses of $LiFePO_4$/C Nanocomposite Cathodes for Lithium Ion Batteries. *J. Phys. Chem. C* **2008**, *112*, 14665−14671.

NOTE ADDED AFTER ASAP PUBLICATION

This paper was published ASAP on July 28, 2023 with an error in the title of Scheme 1. The corrected version was reposted on July 31, 2023.

https://doi.org/10.1021/acs.inorgchem.3c01664
Inorg. Chem. 2023, 62, 12931−12939